High-concentration niobium (V) doping into TiO_2 nanoparticles synthesized by thermal plasma processing

Chenning Zhang
Nano Ceramic Center, National Institute for Materials Science, Tsukuba, Ibaraki 305-0044, Japan; and Department of Environmental Chemistry and Engineering, Tokyo Institute of Technology, Yokohama, Kanagawa 226-8502, Japan

Masashi Ikeda
Nano Ceramic Center, National Institute for Materials Science, Tsukuba, Ibaraki 305-0044, Japan; and Department of Materials Chemistry, Hosei University, Koganei, Tokyo 184-8584, Japan

Tetsuo Uchikoshi
Nano Ceramic Center, National Institute for Materials Science, Tsukuba, Ibaraki 305-0047, Japan

Ji-Guang Li
Nano Ceramic Center, National Institute for Materials Science, Tsukuba, Ibaraki 305-0044, Japan

Takayuki Watanabe
Department of Environmental Chemistry and Engineering, Tokyo Institute of Technology, Yokohama, Kanagawa 226-8502, Japan

Takamasa Ishigaki[a)]
Nano Ceramic Center, National Institute for Materials Science, Tsukuba, Ibaraki 305-0044, Japan; and Department of Chemical Science and Technology, Hosei University, Koganei, Tokyo 184-8584, Japan

(Received 11 October 2010; accepted 10 January 2011)

High-concentration niobium (V)-doped titanium dioxide (TiO_2) nanoparticles of the nonequilibrium chemical composition have been synthesized via Ar/O_2 radio-frequency thermal plasma oxidation of mist precursor solutions with various Nb^{5+} concentrations (Nb/(Ti + Nb) = 0–25.0 at.%). The solubility as high as ~25.0 at.% has not been achieved before by wet-chemical techniques. The preferable anatase formation was attained in the plasma-synthesized powders and was enhanced by the niobium doping. All the powders were heated at high temperatures (600–800 °C) to investigate their phase transformation, band gap variation, inter-particulate binding behavior, and photocatalytic stability. The transformation from anatase to rutile was effectively inhibited by increasing the Nb^{5+} content. The Nb^{5+} doping prevented the band gap of TiO_2 from narrowing after the heating. At high temperatures, Nb^{5+} doping could not only preserve particle size but also prevent inter-particulate binding. High concentration (25.0 at.%) Nb^{5+} doping retained the photocatalytic performance almost invariably irrespective of being thermally treated.

I. INTRODUCTION

Titanium dioxide, TiO_2, as one of the well-known oxide semiconductor materials has been extensively investigated for many applications, such as photocatalysis,[1] solar energy,[2] gas sensors,[3] phosphors,[4] and dilute magnetism,[5] because of its outstanding properties including remarkable chemical and thermal stabilities, high transparency in the visible region, and high refractive index. It usually exists in two polymorphs: anatase (tetragonal, space group:D_{4h}^{19}) and rutile (tetragonal, space group:D_{4h}^{14}). These phases present quite different arrangements of structure-building blocks (Ti–O octahedrons).[6] Specifically, in rutile, each octahedron provides two opposing edges, which are shared to form linear chains along the [001] direction, thus TiO_6 chains are linked to each other via corner connection, whereas anatase has four shared edges per octahedron instead of shared corners, and so the zigzag chains of the octahedrons are linked together via shared edges. Because of the different features of these structures, anatase and rutile exhibit distinctly different properties in terms of theoretical density, refractive index, bandgap, and carrier mobility.[7]

It is well known that metastable anatase, which is considered to have a wider application domain than rutile, transforms to thermodynamically stable rutile at a high temperature above ~500 °C, despite that the exact transformation temperature is affected by many factors such as crystallite size, impurity type and concentration, and atmosphere.[8–10] As a result, nanosized anatase-phase

[a)]Address all correspondence to this author.
e-mail: ishigaki@hosei.ac.jp
DOI: 10.1557/jmr.2011.16

 © Materials Research Society 2011

https://doi.org/10.1557/jmr.2011.16 Published online by Cambridge University Press

TiO_2 with the ability to resist the high temperature treatment will become a highly desired material to yield the high performance. As a typical example, one of the potential applications is that transparent super-hydrophilic TiO_2 coating films on glass or tiles, which give the surface of these substrates a self-cleaning function through utilizing the photocatalytic properties under UV light irradiation,[11,12] require the stable anatase to ensure the higher photocatalytic stability[13] and the kept nanoparticles to improve the high hydrophilic surface[14] after being fired during fabrication process.

Among the countermeasures for nanostructured anatase maintenance used to date, doping niobium into TiO_2 has been effective at impeding anatase-to-rutile transformation and hindering appreciable grain growth. Typically, Ruiz et al.[15,16] have found that the introduction of Nb into TiO_2 retarded the phase transformation at calcination temperatures of 600–900 °C and significantly prevented the particle coarsening, but Nb/Ti atomic ratio via sol–gel synthesis just resided in 0–10%. In addition, recently, Hasegawa and his co-workers[17–21] have successfully fabricated the Nb-doped anatase TiO_2 polycrystalline films with excellent conductivity and transparency, hence opening a paradigm that Nb-doped TiO_2 materials should find the extensive application.

Currently, among the many synthesis techniques for Nb^{5+}-doped TiO_2 powder, wet-chemical techniques are most commonly used.[15,16,22–27] Such techniques, however, may easily produce low crystallinity, nonuniform doping, and hard aggregation via postannealing. In contrast, radio-frequency (RF) thermal plasma processing has been proven to be an effective tool for synthesizing various nanopowders because it has some promising advantages: (i) extremely high synthesis temperature (up to ~15,000 K), (ii) high concentrations of chemically reactive radicals that enhance reactivity, and (iii) superfast quenching rate ($\sim 10^5$–10^6 K/s) in plasma tail flame region.[28,29] In particular, in our previous work, Li et al.[30] have successfully utilized one-step Ar/O_2 RF thermal plasma processing to synthesize highly crystalline TiO_2 powders with controlled phase structures; Wang et al.[31] have shown the other advantage of thermal plasma processing, which gave rise to the nonequilibrium condition in synthesized Fe-doped TiO_2 nanosized powders, that is, quite high-concentration doping; the (Fe/Ti) molar ratio was as high as 0.2 and was attained to form a unique crystal structure composed of ordered oxygen vacancies.

In this work, we have used Ar/O_2 RF thermal plasma to synthesize (0–25.0 at.%) Nb^{5+}-doped TiO_2 nanoparticles through the oxidation of a mist precursor solution containing titanium (IV) tetrabutylate and niobium (V) pentapropylate, and then we have investigated the variation of phase composition, phase transformation from anatase to rutile, inter-particulate binding of the plasma-synthesized powders under high temperatures (600–800 °C), and influence of the heat treatment on photocatalytic stability. We found that solubility of Nb^{5+} into TiO_2 via thermal plasma synthesis reached as high as ~25.0 at.%, which has not been achieved using wet-chemical techniques, and that, for the Nb^{5+}-doped powders at the high temperatures, the transformation from anatase to rutile could be effectively inhibited, crystallite size could be kept almost constant, intercrystalline sintering could be significantly avoided, and high doping concentration (25.0 at.%) saved the photocatalytic property from the influence of the thermal treatment. In the following sections, we report the synthesis process, phase composition, and particle morphology of the plasma-synthesized powders, their variation under the high temperatures, and photocatalytic stability as a function of the heating temperature.

II. EXPERIMENTAL SECTION

A. Synthesis process

All chemicals used in this work were of reagent grade from Wako Pure Chemical Industry Ltd., Osaka, Japan, and were used as received. Liquid precursors were made up of $Ti(OBu)_4$ as titanium (IV) source and $Nb(OBu)_5$ as niobium (V) source, using $HN(OC_2H_5)_2$ (DEA) (in molar ratio, DEA:$Ti(OBu)_4$ = 4:1 and DEA:$Nb(OBu)_5$ = 5:1) to prevent hydrolysis against water or moist air. The nominal addition concentrations of Nb^{5+} in the precursor solutions were varied in the range of Nb/(Ti + Nb) = 0–25.0 at.%.

Experimental apparatus for synthesis of powder was primarily composed of a water-cooled induction plasma torch (model PL-50; Tekna Plasma System Inc., Quebec, Canada), a water-cooled atomizer probe (model SA792-260-100; Tekna Plasma System Inc., Quebec, Canada), a 4-MHz, 40-kW RF power supply system (Nihon Koshuha Co. Ltd., Yokohama, Japan), a water-cooled stainless steel reactor, a stainless steel filter connected to the reactor, and a vacuum pump for adjusting reactor pressure. Details of the experimental setup can be found elsewhere.[30] In this work, the liquid precursors were first delivered by a peristaltic pump and were then injected axially into the plasma reactor as a mist through a probe at the top of the reactor. Experimental conditions for

TABLE I. Experimental conditions for synthesizing the Nb^{5+}-doped TiO_2 nanopowders via the thermal plasma processing.

Parameter	Value
Central gas and flow rate	Ar, 30 L/min
Sheath gas and flow rate	Ar, 80 L/min; O_2, 10 L/min
Atomization gas and flow rate	Ar, 5 L/min
Precursor feeding rate	3.0 mL/min
Induction power for plasma generation	~40 kW
Chamber pressure	~26.7 kPa

https://doi.org/10.1557/jmr.2011.16 Published online by Cambridge University Press

synthesizing the Nb^{5+}-doped TiO_2 nanopowders are summarized in Table I.

B. Heat treatment on the plasma-synthesized nanopowders

All the plasma-synthesized samples were heated in a tube furnace at varying temperatures (600–800 °C) using a digital program controller (model KP 1000; Chino Corporation, Tokyo, Japan) to control temperature rise at 5 °C/min, cooling down at 2 °C/min, and holding time for 3 h.

C. Characterization techniques

Elemental concentrations of Nb^{5+} in all the plasma-synthesized nanopowders were analyzed by an inductively coupled plasma optical emission spectrometer (ICP-OES; model SPS1700HVR, Seiko Instruments Inc. Chiba, Japan).

Oxidation states of titanium and niobium in the plasma-synthesized powders were determined by x-ray photoelectron spectroscopy (XPS) under monochromatized Al Kα irradiation (1486.6 eV) with incident power of 200 W (model XPS 5700; Physical Electronics, Inc., Chanhassen, MN). The core level of Ti $2p_{3/2}$ (458.5 eV) for binding energy was used as a reference to compensate for any possible electrostatic shifts, which are generally caused by the charging of the samples during the photoelectron measurement.

Phase identification was performed via x-ray diffraction (XRD) on a RINT 2200 x-ray diffractometer (Rigaku Corp., Akishima, Tokyo, Japan) using nickel-filtered Cu Kα radiation at 40 kV and 40 mA operation with a scanning speed of 0.5°/2θ per min and was examined via Raman spectroscopy using Ar^+ laser excitation (514.5 nm) with source power of 50 mW and resolution of 1 cm^{-1} (model NR-1800; Jasco Corp., Tokyo, Japan). All the XRD patterns were obtained through the operations of baseline subtraction, Lorentz polarization correction, and $K_{\alpha 2}$ stripping. Rutile weight fractions were calculated from the integrated intensities of the rutile (110) diffraction peaks in the XRD patterns according to an equation derived by Spur and Myers[32]:

$$f_R = \frac{1}{\left(1 + 0.79\frac{I_A}{I_R}\right)} \quad , \tag{1}$$

where f_R is the weight fraction of the rutile and I_R and I_A are the integrated intensities of the rutile (110) and anatase (101) peaks, respectively.

The lattice constants (a and c) in anatase and rutile for the plasma-synthesized powders was evaluated from XRD with a slow scanning speed of 0.25°/2θ per min using mixed high-purity Si powders as an internal standard material according to the formulas given below:

$$a = \frac{\lambda}{2}\sqrt{\frac{l_1^2\left(h_2^2 + k_2^2\right) - l_2^2\left(h_1^2 + k_1^2\right)}{l_1^2 \sin^2\theta_2 - l_2^2 \sin^2\theta_1}} \quad , \tag{2}$$

$$c = \frac{\lambda a l}{\sqrt{4a^2 \sin^2\theta - \lambda^2(h^2 + k^2)}} \quad , \tag{3}$$

where (h,k,l) are the Miller indices, λ is the x-ray wavelength, and θ is the Bragg angle. The diffraction peaks of anatase [(101) and (004)] and rutile [(110) and (111)] were used due to their relatively strong diffraction intensities. The x-ray wavelength using nickel-filtered Cu Kα radiation was taken as 0.15405 nm.

Activation energy for anatase-to-rutile transformation in all the plasma-synthesized powders was estimated from the slope of the plot of the corrected natural log of the calculated rutile weight fraction as a function of the reciprocal of the heat treatment temperature as follows[26]:

$$\ln f_R = -\frac{E_a}{R}\frac{1}{T} \quad , \tag{4}$$

$$E_a = -\frac{\partial \ln(f_R)}{\partial\left(\frac{1}{T}\right)}\frac{R}{1000} \quad , \tag{5}$$

where E_a is the activation energy for the phase transformation, T is the heat treatment temperature in Kelvin, R is the universal gas constant (8.314 J/mol K), and f_R is the rutile weight fraction calculated from Eq. (1).

Ultraviolet–visible (UV–vis) spectra was made on a Jasco V-560 spectrophotometer (Jasco Corp.) using $BaSO_4$ for baseline calibration. Band-gap energies (E_g) were calculated from the UV–vis spectra according to the relationship between the absorption coefficient and incident photon energy for allowed indirect and direct transitions, respectively, given by[33–35]:

$$\begin{aligned} \alpha &= \frac{B_i(h\nu - E_g)^2}{h\nu} \quad \text{(indirect) or} \\ \alpha &= \frac{B_d(h\nu - E_g)^{1/2}}{h\nu} \quad \text{(direct)} \quad , \end{aligned} \tag{6}$$

$$A = \frac{\alpha}{B_i} \quad \text{(indirect) or} \quad A = \frac{\alpha}{B_d} \quad \text{(direct)} \quad , \tag{7}$$

$$h\nu = \frac{1240}{\lambda} \quad , \tag{8}$$

where α is the absorption coefficient, $h\nu$ is the incident photon energy, B_i and B_d are the absorption constants for

https://doi.org/10.1557/jmr.2011.16 Published online by Cambridge University Press

the indirect and direct transitions, respectively, and A is the absorption proportional to α. E_g was obtained by extrapolating the linear parts of the curves in the plots of $(Ahv)^{1/2}$ or $(Ahv)^2$ versus hv.

Particle morphology was observed using field-emission scanning electron microscopy (FE-SEM) (model S-5000; Hitachi Ltd., Tokyo, Japan) and transmission electron microscopy (TEM) (JEM-2000 EX-II; acceleration voltage, 200 kV and JEM-4000 EX; acceleration voltage, 400 kV; JEOLLtd., Tokyo, Japan). Selected area electron diffraction patterns were acquired by JEM-2000 EX-II and high-resolution transmission electron microscopy (HRTEM) was conducted in JEM-4000 EX. Size distributions of particles were then determined from FE-SEM micrographs using an image analyzer software, with d_{50} value taken as average particle size through counting at least 1000 particles in each case.

Specific surface area of the tested powders for photocatalytic performance was determined via Brunauer–Emmett–Teller analysis (Model Belsorp 18; Bell Japan Inc., Tokyo, Japan) with nitrogen chemisorptions at 77 K. Photocatalytic activity was evaluated by bleaching 20 μM of methyl orange ($C_{14}H_{14}N_3NaO_3S$, reagent grade; Wako Pure Chemical Industries Ltd, Osaka, Japan) solution containing the powder catalysts after ultrasonic dispersion under UV light irradiation at room temperature for 2 h. The UV light was generated by UVF–203S Type A light source (San-Ei Electric Co. Ltd; Osaka, Japan) with a composition of five wavelengths of 300, 316, 365, 405, and 436 nm and an intensity ratio of 40:82:100:39:30. The UV light was introduced through a light fiber to illuminate the suspension under agitation with a magnetic bar. The light intensity was adjusted to ~1 mW/cm^2 at the level of the suspension surface. After irradiation, the suspension was centrifuged at 12,000 rounds/min for 30 min using a centrifugal machine for separating the powders from the suspension. The supernatant solution was separated and centrifuged once more to remove the powders as thoroughly as possible. The relative concentration of methyl orange in the recovered solutions was determined by comparing the intensity of 465 nm absorption peak with that of the original methyl orange solution in UV–vis spectra. First of all, a blank test was made to indicate that the methyl orange solution in the absence of any photocatalyst almost had no photocatalytic performance.

III. RESULTS AND DISCUSSION

A. Non-equilibrium chemical composition and anatase phase selection

ICP-OES analysis results (Table II) confirmed that the nominal concentrations of Nb^{5+} in the precursor solutions have almost been retained in the resultant powders. Figure 1 shows XRD patterns of the plasma-synthesized Nb^{5+}-doped TiO_2 powders with various Nb^{5+} concentrations of 0–25.0 at.% (a) before heating, (b) after heating at 600 °C, (c) 700 °C, and (d) 800 °C. Well-defined diffraction peaks were observed for all the samples in Fig. 1(a) because of extremely high synthesis temperature (up to ~15,000 K) in thermal plasma, which would save postannealing step frequently required to obtain good crystallinity in many wet-chemical processes for TiO_2 synthesis.

Oxidation states of niobium and titanium in the plasma-synthesized powders are demonstrated in high-resolution XPS spectra in Figs. 2(a) and 2(b), respectively, using the sample of 6.0 at.% of Nb^{5+} as an example. In Fig. 2(a), the featured peaks of Nb $3d_{5/2}$ and Nb $3d_{3/2}$ located at ~207.8 and ~210.8 eV, respectively, corresponding to the reported values for Nb^{5+} in Nb_2O_5.[36–38] In Fig. 2(b), Ti 2p peaks were found at ~457.9 eV for Ti $2p_{3/2}$ and ~463.8 eV for Ti $2p_{1/2}$ with a spin-orbital doublet splitting (Δ = Ti$2p_{1/2}$-Ti$2p_{3/2}$ = ~5.9 eV), suggesting the presence of Ti in +4.[39,40] Both cases verify that the existences of Nb and Ti in the doped TiO_2 powders as +5 and +4, respectively, have been retained from the precursor solutions due to the effective oxidizing atmosphere in the synthesis process. Considering the oxygen states of niobium and titanium, it can be simply understood that the dominant lattice defects in the Nb-doped TiO_2 should not be the oxygen vacancies, V_O, but interstitial oxygen, O_i, which was formed through a defect reaction:

$$Nb_2O_5 \rightarrow 2Nb^{\bullet}_{Ti} + 4O^{\times}_{o} + O'_i \quad , \qquad (9)$$

where Nb_{Ti}, and O_O denote the niobium ions at titanium site and oxygen ions at oxygen sites, respectively, and symbols, $^{\bullet,x}$ and $'$ are the Kröger–Vink notations for the net charge +1, the zero net charge, and the net charge −1, respectively.[41]

In Fig. 1(a), mixture polymorphs of anatase (JCPDS: No. 84-1286) and rutile (JCPDS: No. 78-2485) could be identified in all the cases. For the phase composition, the metastable anatase appeared as major phase, conforming to our previous theoretical analysis through the calculation on the critical free energy for nucleation,[42] and the anatase composition was increased by the niobium

TABLE II. Elemental concentrations of Nb^{5+} in the plasma-synthesized Nb^{5+}-doped TiO_2 nanopowders.

Nominal concentration in the precursor solutions, Nb/(Nb + Ti) (at.%)	Measured concentration in the synthesized powders, Nb/(Nb + Ti) (at.%)
0.0	0.0
1.0	0.8
6.0	5.8
15.0	15.0
25.0	25.5

https://doi.org/10.1557/jmr.2011.16 Published online by Cambridge University Press

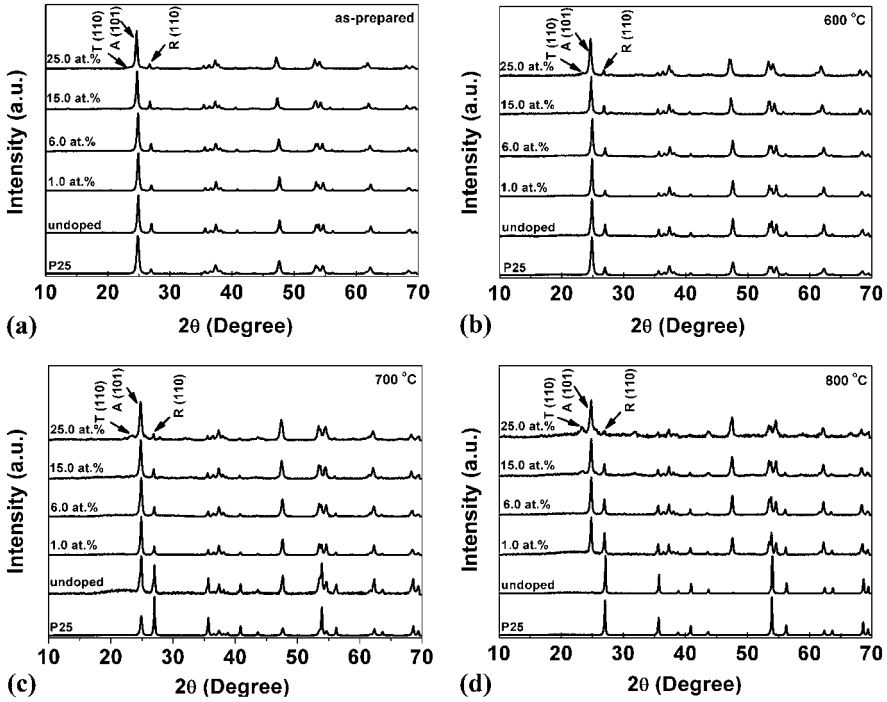


FIG. 1. XRD patterns of the P25 commercial and plasma-synthesized Nb^{5+}-doped TiO_2 powders at various temperatures: (a) before heating, (b) at 600 °C, (c) at 700 °C, and (d) at 800 °C. *A*, *R*, and *T* denote anatase, rutile, and $TiNb_2O_7$, respectively.

doping. Moreover, in Fig. 1(a), relatively weak $TiNb_2O_7$ diffraction peaks (JCPDS: No. 77-1374) could be observed at $2\theta = 23.9°$ in the case of 25.0 at.% of Nb^{5+} doping, indicating that the solubility of Nb^{5+} in the TiO_2 host lattice was limited to ~25.0 at.% in this work. Such a solubility is far higher than those prepared by wet-chemical methods, e.g., ~10.0 at.% via sol–gel route synthesis by Ruiz et al.[15,16] This may be conceivable from thermal plasma processing as a synthesis tool in this experiment, where synthesis temperature of ~15,000 K ensured uniform doping reaction in evaporated state and high concentration of chemically reactive radicals effectively enhanced doping reactivity. To check the dissolubility of Nb^{5+} ions into the TiO_2 host lattice, the lattice constants (*a* and *c*) in anatase and rutile in the plasma-synthesized powders doped with various concentrations of Nb^{5+} (0–25.0 at.%) were measured according to Eqs. (2) and (3) (Fig. 3). The evident change in the lattice constants of two phases at 25.0 at.% case implies that the solubility limit of Nb^{5+} in the TiO_2 host lattice in this study may have been ~25.0 at.%. Such a change might be caused by a radius slightly larger in Nb^{5+} (0.064 nm) than in Ti^{4+} (0.0605 nm)[43] or by the formation of some interstitial oxygen generally due to the valence discrepancy between Nb^{5+} and Ti^{4+}.[44,45] This implication of ~25.0 at.% solubility of Nb^{5+} is consistent with the identification of the $TiNb_2O_7$ diffraction peaks at 25.0 at.% doping content in the XRD patterns [Fig. 1(a)].

The plasma-synthesized powders were recognized to possess the nonequilibrium chemical composition. The Nb^{5+} solubility was reduced to ~15.0 at.% at 800 °C, which could be perceived from the appearance of $TiNb_2O_7$ diffraction peaks in Fig. 1(d), indicating that some Nb^{5+} ions were probably expelled out of the TiO_2 host lattice at this temperature, with a suggestion that the Nb^{5+} solubility was affected by heating temperature. In addition, it can be clearly seen in Figs. 1(b)–1(d) that in the undoped TiO_2 powders, the intensities of the anatase peaks decreased and those of the rutile peaks increased with the raising heating temperature from 600 °C to 800 °C, whereas in the plasma-synthesized Nb^{5+}-doped TiO_2 samples, the intensities of these two phases were not obviously altered by the heating temperature with the increase in doping content, suggesting phase transformation could be effectively inhibited by Nb^{5+} doping.

B. Elevated phase-transformation temperature

To further investigate the inhibition of anatase-to-rutile transformation as a function of Nb^{5+} doping, the variation in rutile weight fraction with heating temperatures was examined, as given in Fig. 4. Before heating, the rutile weight fractions of the plasma-synthesized powders were dependent on the Nb^{5+} addition content, attributable to the charge compensation for Nb^{5+} through the decrease in oxygen vacancies when Nb^{5+} ions were substituted into the TiO_2 lattice,[23] as the formation of rutile was strongly dominated by the number of oxygen vacancies in the TiO_2 lattice.[46] After heating, the increased tendency of the rutile fraction became slower with increasing Nb^{5+}

https://doi.org/10.1557/jmr.2011.16 Published online by Cambridge University Press

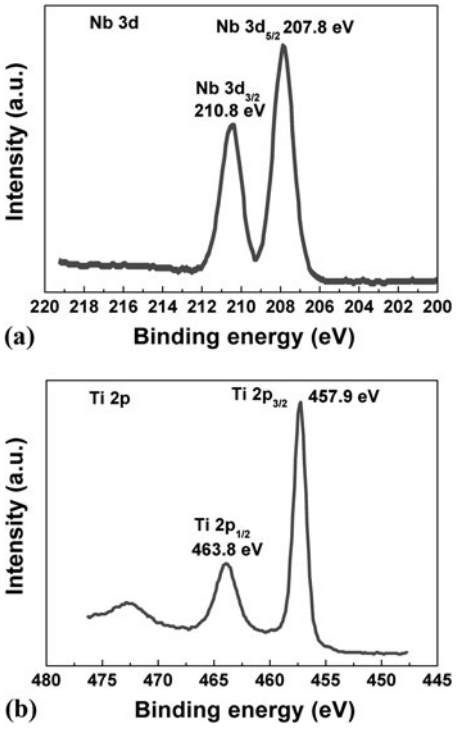


FIG. 2. High-resolution XPS spectra for (a) Nb 3d and (b) Ti 2p in the plasma-synthesized 6.0 at.% Nb^{5+}-doped TiO_2 powders.

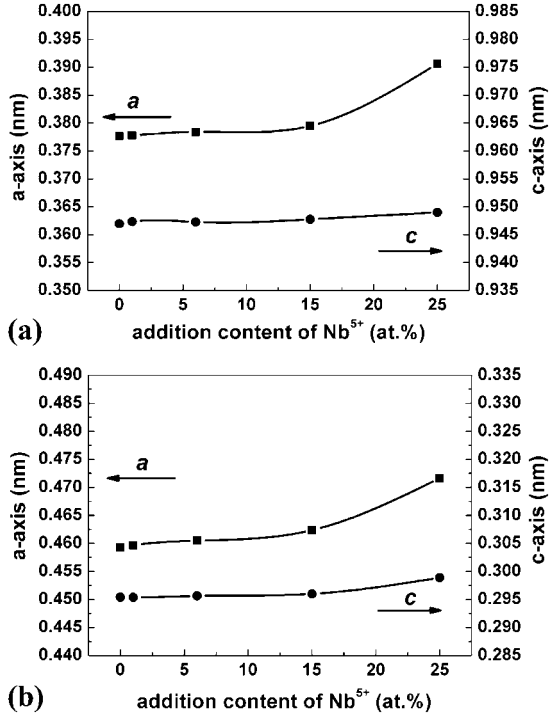


FIG. 3. Variations in the lattice constants (a and c) of (a) anatase and (b) rutile as a function of Nb^{5+} addition content.

concentration. The rutile weight fraction of the undoped TiO_2 calculated from Eq. (1) increased sharply from 22.1 wt% (at 600 °C) to 96.4 wt% (at 800 °C), while that

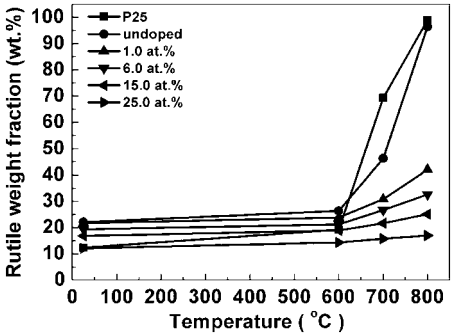


FIG. 4. Variation in the rutile weight fraction of the P25 commercial and plasma-synthesized Nb^{5+}-doped TiO_2 powders after heating.

of 25.0 at.% Nb^{5+}-doped TiO_2 enhanced slightly just from 16.8 wt% (at 600 °C) to 25.1 wt% (at 800 °C), indicating that the anatase-to-rutile transformation could be effectively hindered by the Nb^{5+} doping.

Shannon et al.[9] have found that the phase transformation from anatase to rutile occurring at the surface of bulk anatase was correlated with the high tangential diffusion of anatase nanocrystals, which has later been deduced through molecular dynamics simulations by Ogata et al.[47] Therefore, the inhibition of the phase transformation through the Nb^{5+} doping at the high temperatures in this work might be attributed to the formation of strong Nb-O-Ti bonds that impeded the movement of Ti atoms at the surface of anatase to restrain the phase transformation to rutile. Moreover, there is another factor that influences the phase transformation: as the number of oxygen vacancies acting as nucleation sites for forming rutile transformed from anatase,[48] the smaller number of oxygen vacancies especially at 25.0 at.% Nb^{5+}-doped sample resulting from the introduction of Nb^{5+} into the TiO_2 host lattice via thermal plasma synthesis, as already stated as the reason for the less rutile weight fraction, should be responsible for the decrease in the number of nucleation sites for the phase transformation at the high temperatures.

In our previous works, we synthesized the doped TiO_2 nanoparticles by Ar/O_2 thermal plasma processing using the dopants of Fe^{3+},[31] Eu^{3+},[4] Er^{3+},[49] and Co^{2+}.[5] For all the doped samples, the rutile fraction in the plasma-synthesized powders was increased steadily with the doping concentration. Based on the study of Vemury and Pratsinis[50] on the effect of a dopant on the phase structure of TiO_2 powders obtained via flame pyrolysis, who found that the rutile formation was enhanced by creating the oxygen vacancies in the gas clusters by doping with subvalent cations such as Al^{3+}, the introduction of metal cations of Fe^{3+}, Eu^{3+}, Er^{3+}, and Co^{2+} having lower chemical valence than Ti^{4+} into the TiO_2 host lattice via thermal plasma processing, which has similarities to the flame pyrolysis approach, gave rise to creation of oxygen vacancies for charge compensation in the TiO_2 gas clusters at the high temperature of thermal plasma and therefore

https://doi.org/10.1557/jmr.2011.16 Published online by Cambridge University Press

promoted the rutile formation. Moreover, Barakat and Shah[51] reported that the ratio of rutile to anatase was raised with increasing Co^{2+} doping concentration at the same annealing temperature. This indicates that the formed oxygen vacancies resulting from the charge discrepancy between Co^{2+} and Ti^{4+} should be responsible for the inferior stability of the phase transformation by acting as nucleation sites for the rutile crystallization. In contrast, in our study, the formation of the oxygen vacancies as the rutile nucleation sites were inhibited by the Nb^{5+} doping into the TiO_2 host lattice, due to the contribution of charge compensation from the higher chemical valence of Nb^{5+} than that of +4, therefore, resulting in the better stability of the anatase-to-rutile phase transformation compared to the cases stabilized with the other dopants with lower chemical valence when heating at high temperature. Such result is consistent with the finding reported by Guidi et al.,[24] that is, for the doped TiO_2 samples prepared by spray pyrolysis, in the temperature range of 750–850 °C, Ga^{3+}-doped titania featured a transformation of 75% anatase to rutile, whereas the percentage of conversion was about 45% for Nb^{5+}-doped samples.

Besides, in contrast to the rutile weight fractions (42.7 wt% at 700 °C and 87.1 wt% at 800 °C) in 1.0 at.% Nb^{5+}-doped TiO_2 via sol–gel synthesis by Ahmad et al.,[26] the counterparts with the same Nb^{5+} doping concentration via thermal plasma synthesis in this study of 30.8 wt% at 700 °C and 42.0 wt% at 800 °C, are appreciably lower than them. In the Nb-doped TiO_2 sensing films with a wide range of Nb contents (0–10 at.%) synthesized using the sol–gel route by Ruiz et al.[15] at calcination temperature of 700 °C, the conversion efficiency of anatase-to-rutile transformation is 14% at doping concentration of 6.0 at.%, which was considered to make the saturated effect on the phase transition, namely, the percentage of phases was very similar at each calcination temperature owing to the $TiNb_2O_7$ formation at content of higher than 6 at.%. In comparison with this case, the plasma-synthesized 6.0 at.% Nb^{5+}-doped TiO_2 powders in this work, under the same heating temperature of 700 °C, the conversion efficiency of the phase transformation is just 7.3% (from 19.4 wt% in the as-prepared sample to 26.7 wt% in the 700 °C-heated one, as demonstrated in Fig. 4), which is less than 14% of the phase conversion efficiency in the Nb-doped TiO_2 films. This indicates that the incorporation of Nb into TiO_2 lattice upon the thermal plasma technique probably yielded more homogeneous doping distribution through the reaction in the evaporated state than upon the sol–gel synthesis due to the extremely high synthesis temperature of ~15,000 K of the thermal plasma. Furthermore, such conversion efficiency is 3.7% at high Nb doping addition of 25.0 at.% (Fig. 4), indicating that more effective stability on anatase phase when heating at high temperature can be achieved by doping high concentration of Nb using the thermal plasma processing. For the comparison with Degussa P25 commercial powder (Nippon Aerosil, Tokyo, Japan), XRD patterns [Figs. 1(a)–1(d)] in conjunction with Raman spectra [Figs. 6(a)–6(d)] unambiguously reveal that the anatase composition was decreased with raising heating temperature by identifying the relative intensities of the anatase and rutile peaks. Especially, at 800 °C, most of the anatase in the P25 powder was transformed to the rutile upon the heating treatment, quite like the case in the undoped TiO_2 powder. In contrast, such phase transformation in the Nb-doped TiO_2 powders is not readily to be discerned. This suggests that the anatase stability is poor in both the powders of P25 and undoped TiO_2 when heating at the high temperature. Through the calculation of the rutile weight fraction in the phase composition (Fig. 4), it was found that the rutile weight fraction of the P25 powder was appreciably increased from 12.3 wt% as as-received powder to 98.9 wt% after heating at 800 °C, with a conversion efficiency of 86.6%, which is slightly higher than 73.9% in the undoped TiO_2, but is far less than 4.9% in the 25.0 at.% Nb^{5+}-doped TiO_2. This is indicative of the fact that high-concentration Nb doping into TiO_2 can significantly improve the anatase stability, despite being treated at high temperature, which is also evidenced by their discrepant activation energies, calculated from Eqs. (4) and (5), of the phase transformation of 58 KJ/mol for the undoped sample and 93 KJ/mol for 25.0 at.% Nb^{5+}-doped TiO_2 in Fig. 5. The enhanced activation energy with increasing Nb^{5+} concentration indicates that the higher the Nb^{5+} content was, the higher the temperature required for completing the transformation. Although the accuracy of the calculation of activation energy was not high, due to relatively few heating temperatures (three temperatures: 600, 700, and 800 °C) in this work, a tendency of the increase in the activation energy with the addition of $Nb^{5+}$was still found. In this case, heavier Nb^{5+} doping made such a transformation more difficult to progress upon breaking Nb–O–Ti bond.

Figure 6 exhibits Raman spectra of the plasma-synthesized Nb^{5+}-doped TiO_2 samples with various Nb^{5+}

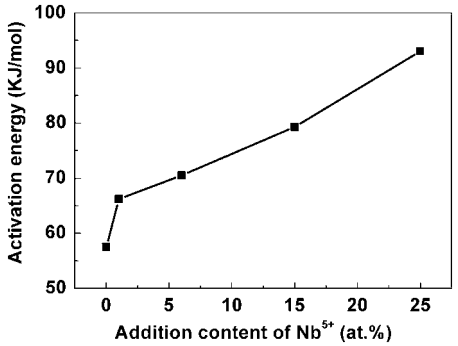


FIG. 5. Activation energy for the anatase-to-rutile transformation in the plasma-synthesized Nb^{5+}-doped TiO_2 powders as a function of Nb^{5+} addition content.

https://doi.org/10.1557/jmr.2011.16 Published online by Cambridge University Press

concentrations of 0–25.0 at.% (a) before heating, (b) after heating at 600 °C, (c) 700 °C, and (d) 800 °C. Because the structures of anatase and rutile of TiO_2 are very sensitive to Raman scattering, Raman spectra can provide valuable characterization information upon the phase composition of the samples. Figure 6(a) shows that all the powders synthesized by thermal plasma were composed of mixture polymorphs of main-phase anatase and rutile on the basis of the fundamental vibrational modes,[52] as indicated in the Raman spectra, which are in good agreement with the identification in the XRD patterns [Fig. 1(a)], but the presence of $TiNb_2O_7$ Raman band was overlapped by strong TiO_2 Raman bands due to its quite weak scattering intensity. Among these fundamental vibrational modes, two Raman bands $A(E_g)$ (~145 cm^{-1}) for anatase and $R(E_g)$ (~446 cm^{-1}) for rutile, as indicated by dashed lines in the spectra, are frequently used to characterize the variation in phase composition.[53] Thus, in the sequence from Figs. 6(b) to 6(d), the intensities of the characteristic $A(E_g)$ modes for anatase in the undoped TiO_2 reduced and those of the $R(E_g)$ modes for rutile enhanced when heating temperature was elevated from 600 to 800 °C, whereas those in the Nb^{5+}-doped TiO_2 were not appreciably altered especially for the case of high doping concentration of 25.0 at.% at the same condition. This is also consistent with the result in the XRD analysis very well [Figs. 1(b)–1(d)], indicating that the phase transformation could be effectively inhibited by the Nb^{5+} doping.

Figure 7(a) shows the absorption spectra of the undoped and 15.0 at.% Nb^{5+}-doped TiO_2 powders before and after heating at 800 °C, as representative cases for comparison. From this figure, it is hard to distinguish any obvious difference between the absorption onsets of these two powders before heating, but there is an obvious difference between them after heating at 800 °C, that is, the absorption onset in the undoped sample after heating occurred unambiguously redshift compared with that in the case of 15.0 at.% Nb^{5+} doping, suggesting that the Nb^{5+} doping prevented the band gap (E_g) of TiO_2 from narrowing after heating. Consequent evidence for this suggestion can be found in Figs. 7(b) and 7(c), which show the indirect and direct E_g estimated from the UV–vis spectra [Fig. 7(a)] according to Eqs. (6)–(8), respectively. Semiconductors are classified as direct or indirect according to the lowest allowed electronic transition. The direct semiconductors are characterized by the minimum of the lowest conduction band positioned in k space directly under the maximum of the highest valence band, whereas for the indirect semiconductors, the minimum of the lowest conduction band is shifted relative to the maximum of the highest valence band and the lowest-energy interband transition must then be accompanied by phonon excitation.[54] Even though TiO_2 has generally been known to be an indirect semiconductor,[55–57] both the indirect and direct interband transitions can occur simultaneously under irradiation with sufficient energy[58] and can be distinguished by their

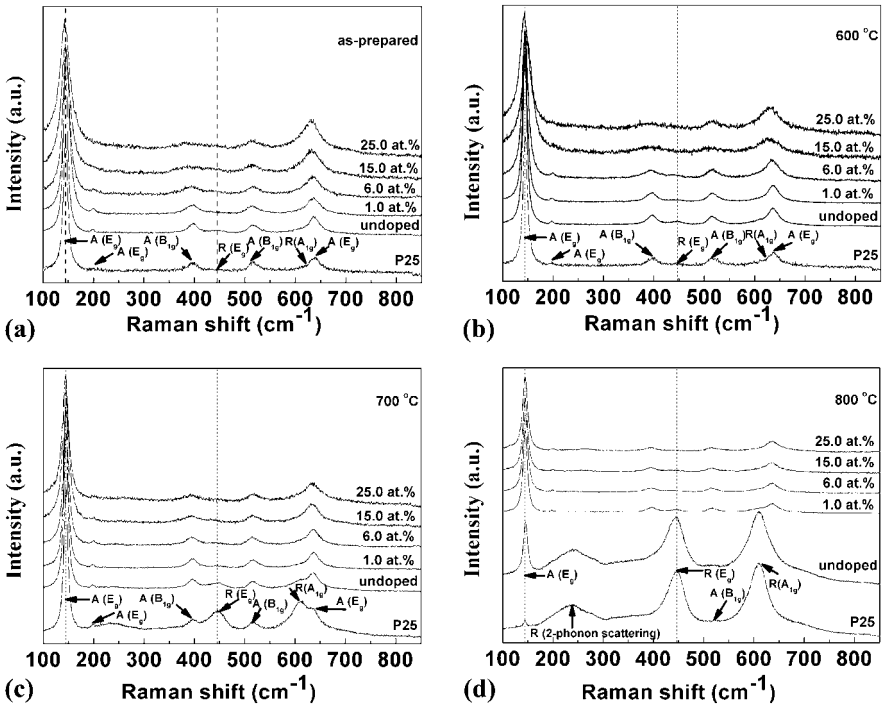


FIG. 6. Raman spectra of the P25 commercial and plasma-synthesized Nb^{5+}-doped TiO_2 powders at various temperatures: (a) before heating, (b) at 600 °C, (c) at 700 °C, and (d) at 800 °C. *A* and *R* denote anatase and rutile, respectively. Characteristic Raman bands of *A* (E_g) and *R* (E_g) are marked with dashed lines.

https://doi.org/10.1557/jmr.2011.16 Published online by Cambridge University Press

energy dependence of the optical absorption edge,[35] as expressed by Eqs. (6)–(8) for E_g estimation. The verification of the estimation accuracy has previously been preceded by using Degussa P25 TiO_2 powder.[59] The equations mentioned above have been used in our previous work of the Fe^{3+}-doped TiO_2 nanopowders synthesized in thermal plasma, with the mixture polymorphs of anatase and rutile, to estimate the indirect and direct band gap energies, respectively.[31] The estimated results in this work are presented in Fig. 7(b) for the indirect transition and in Fig. 7(c) for the direct transition. For the indirect band gap, E_g of the undoped TiO_2 was narrowed to ~2.67 eV after the heating from ~2.76 eV before the heating, with ΔE_g = ~−0.09 eV, and the variation of that in the 15.0 at.% Nb^{5+}-doped TiO_2 was ~−0.03 eV, ΔE_g = ~2.74–~2.77 eV, whereas for the direct band gap, after the thermal treatment, such E_g variation (ΔE_g) for the undoped sample was ~−0.10 eV (from ~3.09 to ~2.99 eV) and the narrowed E_g for the 15.0 at.% Nb^{5+}-doped case was ~3.07 eV, with ΔE_g = ~−0.03 eV (from ~3.10 to ~3.07 eV). The evaluations of the E_g variation for the indirect and direct interband transitions claimed that the Nb^{5+} doping made a contribution in the band gap preservation for the TiO_2 host lattice when being thermally heated. The probable explanation for the narrowing prevention of the band gap resulting from Nb^{5+} doping is that, when Nb^{5+} was introduced into TiO_2 host lattice, the adjacent Nb_{Ti}–V_O and Nb_{Ti}–O_i structures induced impurity states in the band gap and the Nb atom could stabilize the impurity state.[44] In this case, the stabilized impurity state might be responsible for the band gap preservation from heating.

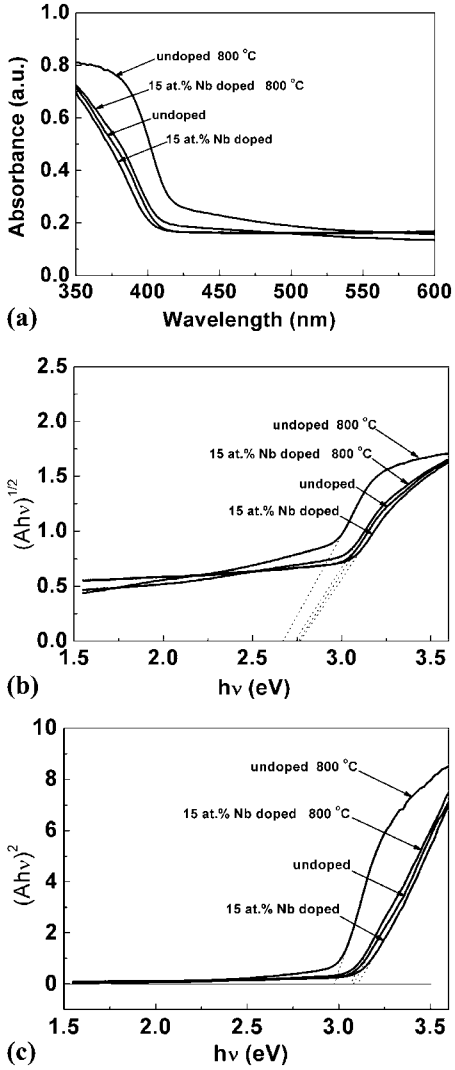


FIG. 7. UV–vis absorption spectra of the undoped and 15.0 at.% Nb^{5+}-doped TiO_2 powders synthesized via (a) the thermal plasma processing before and after heating at 800 °C, correspondingly estimated (b) indirect and (c) direct band gap energies (E_g).

C. Variation in particle morphology

FE-SEM observation of particle morphologies of some plasma-synthesized powders as typical cases before and after heating are illustrated in Fig. 8 for comparison: (a) undoped TiO_2, (b) undoped TiO_2 at. 800 °C, (c) 15.0 at.% Nb^{5+}-doped TiO_2, (d) 15.0 at.% Nb^{5+}-doped TiO_2 at 800 °C, (e) 25.0 at.% Nb-doped TiO_2, and (f) 25.0 at.% Nb^{5+}-doped TiO_2 at 800 °C. In the plasma-synthesized samples before heating [Figs. 8(a), 8(c), and 8(e)], a majority of nanosized particles (several nanometers) assumed faceted shape and a small proportion of submicrometer ones (~100 nm) appeared as rough sphere. Such a characteristic morphology was more readily perceived from the TEM micrographs of the undoped and 15.0 at.% Nb^{5+}-doped TiO_2 samples in Figs. 9(a) and 10(a). The possible particle formation pathways for the morphology are as follows: the fine particles were produced via a gas–solid course, whereas the large ones were formed via a gas–liquid–solid route. In addition, there exists an interesting morphology in the 15.0 at.% Nb^{5+}-doped TiO_2 [Fig. 10(c)]: a small anatase nanocrystal was found to use a shared surface with a large rutile particle by identifying *d* space from HRTEM observation of individual particle, which has seldom been reported for solution-based methods. This intergrown morphology confirms that small anatase crystals should be formed in a rapid cooling process while large rutile particles should be created in a less cooling condition, which is conforming to the our previous thermodynamic analysis of nucleation of anatase and rutile from TiO_2 melt.[42] In contrast, it should be noted that this intergrown morphology is different from the case of the separated rutile structure in the approximately parallel lamellae of the crystallographic shear (CS) planes in Fe^{3+}-doped TiO_2 via thermal plasma synthesis.[31] In the case of Fe^{3+} doping, the intergrown morphology is attributed to the concentrated oxygen deficiencies originating from Fe^{3+} addition within these CS planes when atomic ratio ($R_{Fe/Ti}$) reached a maximum value of 2%. On

https://doi.org/10.1557/jmr.2011.16 Published online by Cambridge University Press

the other hand, in this study, the oxygen vacancies as deficiencies was reduced by charge compensation owing to Nb^{5+} doping, as proved by the estimation of rutile weight fraction (Fig. 4), causing little possibility of the formation of concentrated oxygen deficiencies.

After heating at 800 °C, the particle morphologies of these samples underwent significant changes, as seen in Figs. 8(a)–8(f). Some apparent sintering trace among particles occurred after heating the undoped TiO_2 powders [Fig. 8(b)] with appreciable grain growth from d_{50} = 33 nm before heating to d_{50} = 75 nm after heating, as seen from their size distributions in Figs. 11(a) and 11(b). TEM observation [Fig. 9(b)] unambiguously revealed the occurrence of sintering phenomenon between two particles (indicated by a white arrow) in the undoped TiO_2 powders. On the other hand, at the same heating temperature, in the 15.0 at.% Nb^{5+} case, the intergranular sintering was weak [Figs. 8(d) and 10(b)] and the variation in crystallite size was merely from d_{50} = 55 nm to d_{50} = 61 nm [Figs. 11(c) and 11(d)], and particularly, this variation in 25.0 at.% Nb^{5+} sample was held almost invariable [(d_{50} = 60 nm before heating and d_{50} = 61 nm after heating, Figs. 11(e) and 11(f)]. According to the findings of Sharma et al.,[60] substitutional Nb^{5+} could induce slight stress in the TiO_2 lattice as a result of the slightly bigger ionic radius of Nb^{5+} (0.064 nm) than that of Ti^{4+} (0.0605 nm) to hinder the crystallite growth upon heating as a contribution from Nb^{5+} doping. The induced slight stress caused by Nb^{5+} substitution should be raised with the doping concentration, which is responsible for significant effect of the high doping concentration of 25.0 at.% on the growth inhibition.

D. Photocatalytic stability

For the photocatalytic measurement, we used the P25 commercial powder, which has been a standard material in the field of the photocatalytic reactions, and

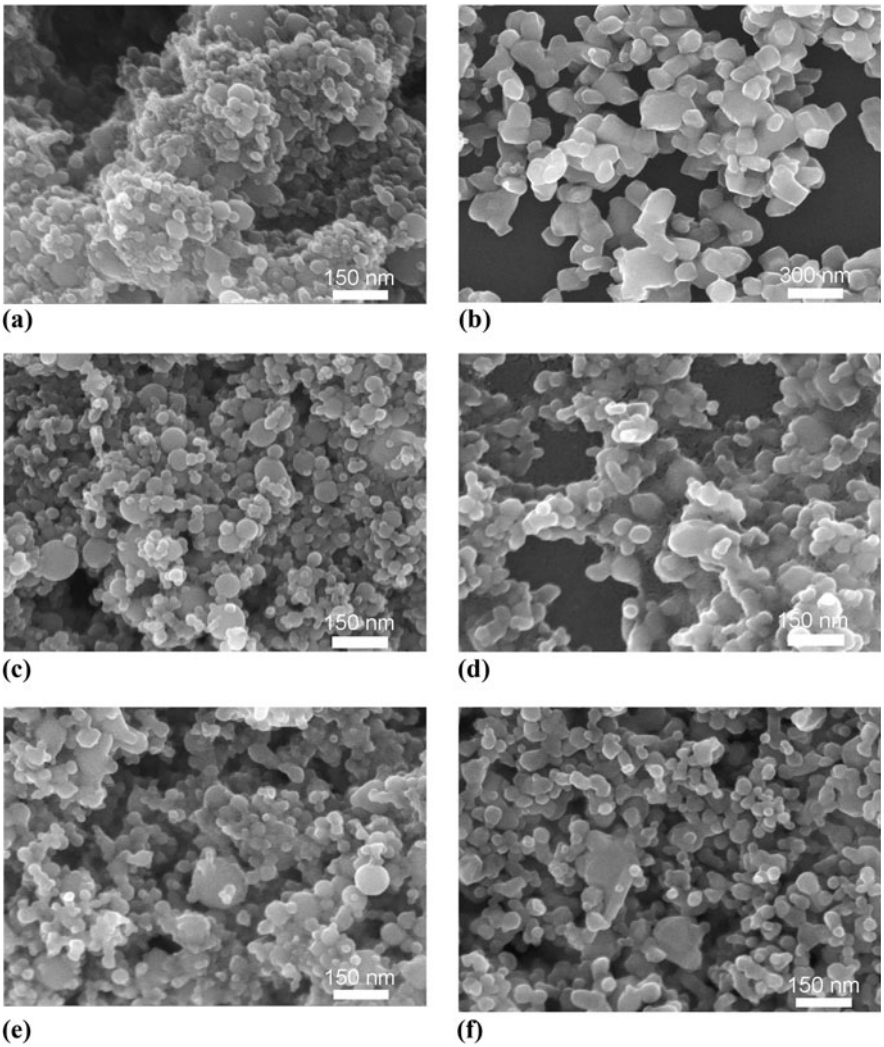


FIG. 8. FE-SEM micrographs showing the overall morphologies of some plasma-synthesized Nb^{5+}-doped TiO_2 powders: (a) 0 at.% of Nb^{5+}, (b) 0 at.% of Nb^{5+} at 800 °C, (c) 15.0 at.% of Nb^{5+}, (d) 15.0 at.% of Nb^{5+} at 800 °C, (e) 25.0 at.% of Nb^{5+}, and (f) 25.0 at.% of Nb^{5+} at 800 °C.

https://doi.org/10.1557/jmr.2011.16 Published online by Cambridge University Press

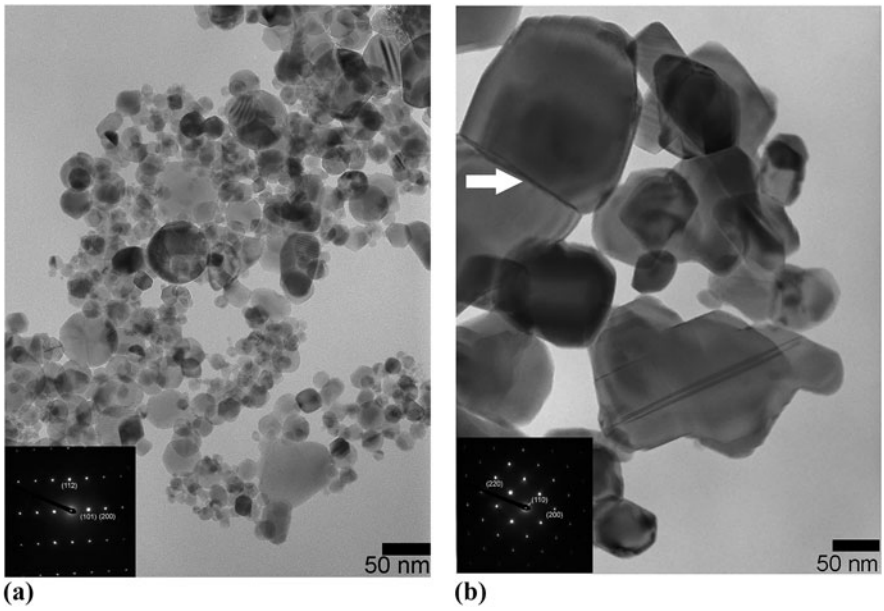


FIG. 9. TEM micrographs showing the morphology of the plasma-synthesized undoped TiO_2 powders: (a) before heating and (b) after heating at 800 °C. Electron-diffraction patterns for individual anatase and rutile crystals are exhibited in the insets, respectively. White arrow indicates sintering between two particles.

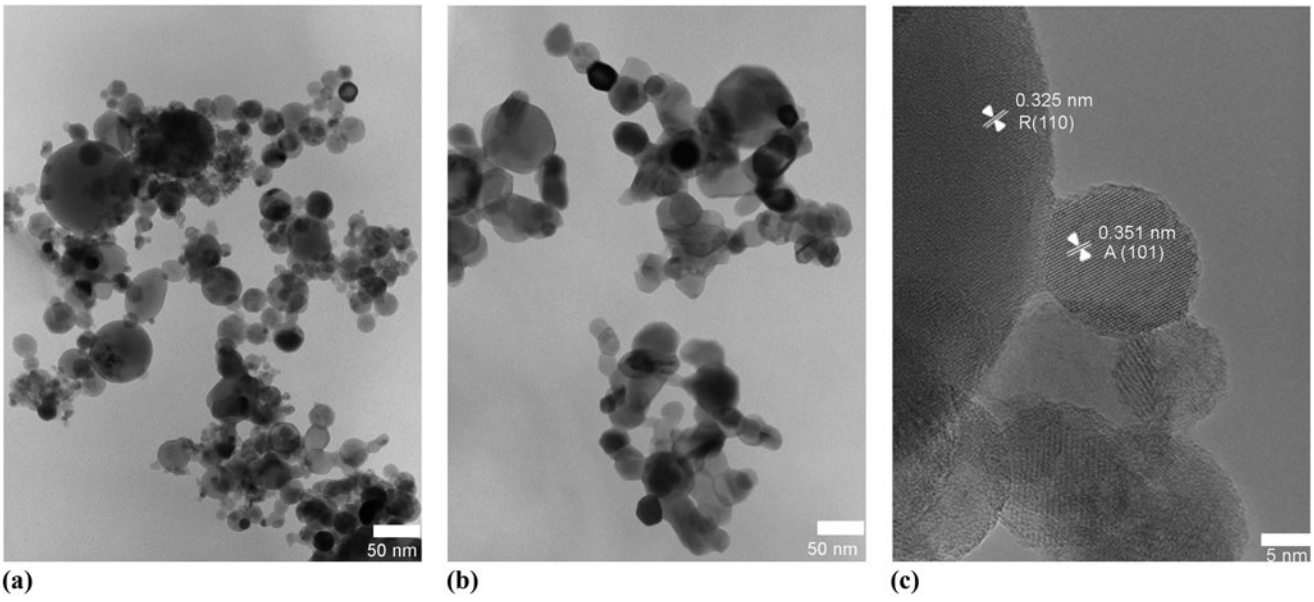


FIG. 10. TEM micrographs showing the morphology of the plasma-synthesized 15.0 at.% Nb^{5+}-doped TiO_2 powders: (a) before heating, (b) after heated at 800 °C, and (c) HRTEM lattice fringes of individual anatase and rutile particles.

plasma-synthesized powders of undoped and 25.0 at.% Nb^{5+}-doped TiO_2 as catalyst. The photocatalytic performance is a delicate function of many factors, among which specific surface area plays an important role in the migration survival from the crystallite interior to surfaces for free h^+/e^-.[61] Thus, to exclude the effects of specific surface area, the surface area of all the tested powders was set as 0.125 m^2 by varying the sample weight, according to their specific surface areas for P25 (~50 m^2/g), undoped TiO_2 (~46 m^2/g), and 25.0 at.% Nb^{5+}-doped TiO_2 (~25 m^2/g). Figure 12 shows relative concentration variation of the methyl orange using the catalysts of P25, undoped, and 25.0 at.% Nb^{5+}-doped TiO_2 powders after UV irradiation for 2 h as a function of heating temperature (600–800 °C), revealing the influence of the heat treatment on their photocatalytic performance. It was found that although the as-received

https://doi.org/10.1557/jmr.2011.16 Published online by Cambridge University Press

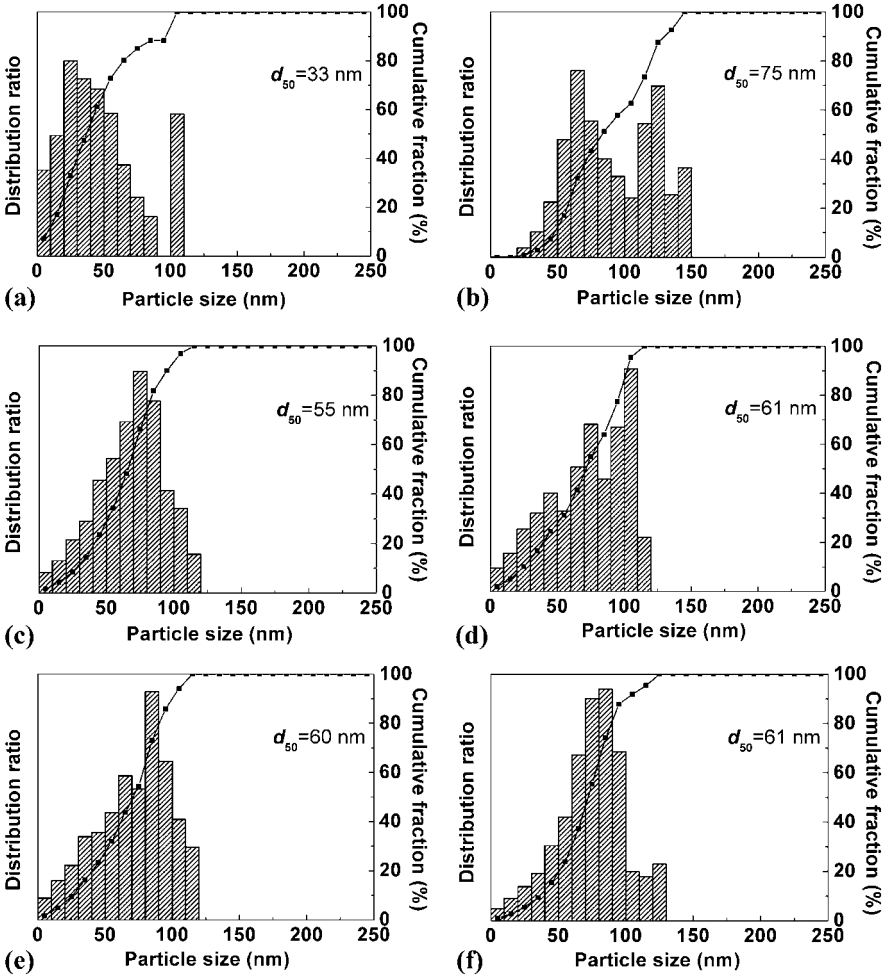


FIG. 11. Size distributions of the plasma-synthesized Nb^{5+}-doped TiO_2 powders: (a) 0 at.% of Nb^{5+}, (b) 0 at.% of Nb^{5+} at 800 °C, (c) 15.0 at.% of Nb^{5+}, (d) 15.0 at.% of Nb^{5+} at 800 °C (e) 25.0 at.% of Nb^{5+}, and (f) 25.0 at.% of Nb^{5+} at 800 °C.

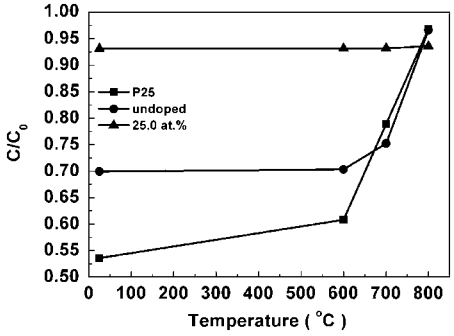


FIG. 12. Relative concentration variation of the methyl orange using the catalysts of P25, undoped, and 25.0 at% Nb^{5+}-doped TiO_2 powders after UV irradiation for 2 h as a function of heating temperature (600–800 °C).

P25 commercial powder has the superior photocatalytic performance to the as-prepared 25.0 at.% Nb^{5+}-doped TiO_2 powder, the performance of the P25 powder after being thermally treated at 600–800 °C decayed quite sharply, which could also be disclosed similarly for the undoped case after the treatment. On the other hand, by unambiguous comparison, 25.0 at.% Nb^{5+}-doped sample retained its photocatalytic activity almost invariably, even though being heated at the high temperature. At 800 °C, the doped sample even possessed better performance than both the powders of P25 and undoped. This implies that the high Nb doping concentration saved the photocatalytic property from the influence of the thermal treatment, which is mainly understood from the advantage of anatase phase stability, as shown in Fig. 4. It has been known that the anatase is more active in the photocatalysis, which is probably ascribed to higher Fermi level and less surface hydroxylation.[13,62] Therefore, high stability of the anatase after heat treatment is of importance to the photocatalytic performance.

IV. CONCLUSIONS

Nb (V)-doped TiO_2 nanopowders have been synthesized via Ar/O_2 RF thermal plasma oxidation mist precursor solutions, with doping concentrations (solubility)

https://doi.org/10.1557/jmr.2011.16 Published online by Cambridge University Press

as high as ~25.0 at.%. All the plasma-synthesized powders comprised mixture polymorph of anatase (major phase), ~80 mass%, and rutile, whereas higher Nb^{5+} contents could effectively inhibit anatase-to-rutile transformation and preserve the band gap of TiO_2 under high temperature. At high temperatures, Nb^{5+} doping could play an important role not only in restraining nanoparticle growth but also in avoiding binding between crystallites. High doping concentration (25.0 at.%) saved the photocatalytic performance from the influence of thermal treatment, mainly due to its advantage of anatase phase stability. This work might be an exploration in understanding TiO_2 doped with other transition metal elements and might find the potential applications for TiO_2 semiconductor materials in some high-temperature working environments.

ACKNOWLEDGMENTS

The authors are grateful to our colleagues at NIMS, Mr. Yoshiyuki Yajima and Mr. Satoshi Takenouchi, for their chemical analysis of the synthesized nanosized powders. This work was partially supported by KAKENHI, a Grant-in-Aid for Scientific Research (B 19360334) from the Japan Society for the Promotion of Science.

REFERENCES

1. T.N. Obee and R.T. Brown: TiO_2 photocatalysis for indoor air applications-effects of humidity and trace contaminant lels on the oxidation rates of formaldehyde, toluene, and 1,3-butadiene. *Environ. Sci. Technol.* **29**, 1223 (1995).
2. G.K. Mor, O.K. Varghese, M. Paulose, K. Shankar, and C.A. Grimes: A review on highly ordered, vertically oriented TiO_2 nanotube arrays: Fabrication, material properties, and solar energy applications. *Sol. Energy Mater. Sol. Cells* **90**, 2011 (2006).
3. A.M. Ruiz, A. Cornet, K. Shimanoe, J.R. Morante, and N. Yamazoe: Effects of various metal additives on the gas sensing performances of TiO_2 nanocrystals obtained from hydrothermal treatments. *Sens. Actuators, B* **108**, 34 (2005).
4. J.G. Li, X.H. Wang, K. Watanabe, and T. Ishigaki: Phase structure and luminescence properties of Eu^{3+}-doped TiO_2 nanocrystals synthesized by Ar/O_2 radio frequency thermal plasma oxidation of liquid precursor mists. *J. Phys. Chem. B* **110**, 1121 (2006).
5. J.G. Li, R. Buechel, M. Isobe, T. Mori, and T. Ishigaki: Cobalt-doped TiO_2 nanocrystallites: Radio-frequency thermal plasma processing, phase structure, and magnetic properties. *J. Phys. Chem. C* **113**, 8009 (2009).
6. A.F. Wells: *Structural Inorganic Chemistry* (Clarendon Press, Oxford, 1975).
7. T. Fukumura, H. Toyosaki, and Y. Yamada: Magnetic oxide semiconductors. *Semicond. Sci. Technol.* **20**, S103 (2005).
8. Y. Hu, H.L. Tsai, and C.L. Huang: Phase transformation of precipitated TiO_2 nanoparticles. *Mater. Sci. Eng. A-Struct.* **344**, 209 (2003).
9. R.D. Shannon and J.A. Pask: Kinetics of anatase-rutile transformation. *J. Am. Ceram. Soc.* **48**, 391 (1965).
10. F.C. Gennari and D.M. Pasquevich: Kinetics of the anatase rutile transformation in TiO_2 in the presence of Fe_2O_3. *J. Mater. Sci.* **33**, 1571 (1998).
11. T. Watanabe, A. Nakajima, R. Wang, M. Minabe, S. Koizumi, A. Fujishima, and K. Hashimoto: Photocatalytic activity and photoinduced hydrophilicity of titanium dioxide coated glass. *Thin Solid Films* **351**, 260 (1999).
12. I. Sopyan, S. Murasawa, K. Hashimoto, and A. Fujishima: Highly efficient TiO_2 film photocatalyst-degradation of gaseous acetaldehyde. *Chem. Lett.* **23**, 723 (1994).
13. K. Tanaka, M.F.V. Capule, and T. Hisanaga: Effect of crystallinity of TiO_2 on its photocatalytic action. *Chem. Phys. Lett.* **187**, 73 (1991).
14. R. Wang, K. Hashimoto, A. Fujishima, M. Chikuni, E. Kojima, A. Kitamura, M. Shimohigoshi, and T. Watanabe: Light-induced amphiphilic surfaces. *Nature*. **388**, 431 (1997).
15. A.M. Ruiz, G. Dezanneau, J. Arbiol, A. Cornet, and J.R. Morante: Study of the influence of Nb content and sintering temperature on TiO_2 sensing films. *Thin Solid Films* **436**, 90 (2003).
16. A.M. Ruiz, G. Dezanneau, J. Arbiol, A. Cornet, and J.R. Morante: Insights into the structural and chemical modifications of Nb additive on TiO_2 nanoparticles. *Chem. Mater.* **16**, 862 (2004).
17. N.L.H. Hoang, N. Yamada, T. Hitosugi, J. Kasai, S. Nakao, T. Shimada, and T. Hasegawa: Low-temperature fabrication of transparent conducting anatase Nb-doped TiO_2 films by sputtering. *Appl. Phys. Express*. **1**, 115001 (2008).
18. N. Yamada, T. Hitosugi, N.L.H. Hoang, Y. Furubayashi, Y. Hirose, S. Konuma, T. Shimada, and T. Hasegawa: Structural, electrical and optical propel-ties of sputter-deposited Nb-doped TiO_2 (TNO) polycrystalline films. *Thin Solid Films* **516**, 5754 (2008).
19. T. Hitosugi, H. Kamisaka, K. Yamashita, H. Nogawa, Y. Furubayashi, S. Nakao, N. Yamada, A. Chikamatsu, H. Kumigashira, M. Oshima, Y. Hirose, T. Shimada, and T. Hasegawa: Electronic band structure of transparent conductor: Nb-doped anatase TiO_2. *Appl. Phys. Express*. **1**, 111203 (2008).
20. Y. Hirose, N. Yamada, S. Nakao, T. Hitosugi, T. Shimada, and T. Hasegawa: Large electron mass anisotropy in a d-electron-based transparent conducting oxide: Nb-doped anatase TiO_2 epitaxial films. *Phys. Rev. B* **79**, 165108 (2009).
21. T. Hitosugi, N. Yamada, N.L.H. Hoang, J. Kasai, S. Nakao, T. Shimada, and T. Hasegawa: Fabrication of TiO_2-based transparent conducting oxide on glass and polyimide substrates. *Thin Solid Films* **517**, 3106 (2009).
22. E. Traversa, M.L. Di Vona, S. Licoccia, M. Sacerdoti, M.C. Carotta, L. Crema, and G. Martinelli: Sol-gel processed TiO_2-based nano-sized powders for use in thick-film gas sensors for atmospheric pollutant monitoring. *J. Sol-Gel Sci. Technol.* **22**, 167 (2001).
23. J. Arbiol, J. Cerda, G. Dezanneau, A. Cirera, F. Peiro, A. Cornet, and J.R. Morante: Effects of Nb doping on the TiO_2 anatase-to-rutile phase transition. *J. Appl. Phys.* **92**, 853 (2002).
24. V. Guidi, M.C. Carotta, M. Ferroni, G. Martinelli, and M. Sacerdoti: Effect of dopants on grain coalescence and oxygen mobility in nanostructured titania anatase and rutile. *J. Phys. Chem. B* **107**, 120 (2003).
25. M. Sacerdoti, M.C. Dalconi, M.C. Carotta, B. Cavicchi, M. Ferroni, S. Colonna, and M.L. Di Vona: XAS investigation of tantalum and niobium in nanostructured TiO_2 anatase. *J. Solid State Chem.* **177**, 1781 (2004).
26. A. Ahmad, S. Buzby, C. Ni, and S.I. Shah: Effect of Nb and Sc doping on the phase transformation of sol-gel processed TiO_2 nanoparticles. *J. Nanosci. Nanotechnol.* **8**, 2410 (2008).
27. A. Ahmad, J.A. Shah, S. Buzby, and S.I. Shah: Structural effects of codoping of Nb and Sc in titanium dioxide nanoparticles. *Eur. J. Inorg. Chem. 948* (2008).
28. T. Ishigaki and J.G. Li: Synthesis of functional TiO_2-based nanoparticles in radio frequency induction thermal plasma. *Pure Appl. Chem.* **80**, 1971 (2008).

https://doi.org/10.1557/jmr.2011.16 Published online by Cambridge University Press

29. T. Ishigaki: Synthesis of ceramic nanoparticles with non-equilibrium crystal structures and chemical compositions by controlled thermal plasma processing. *J. Ceram. Soc. Jpn.* **116**, 1351 (2008).
30. Y.L. Li and T. Ishigaki: Controlled one-step synthesis of nanocrystalline anatase and rutile TiO_2 powders by in-flight thermal plasma oxidation. *J. Phys. Chem. B* **108**, 15536 (2004).
31. X.H. Wang, J.G. Li, H. Kamiyama, M. Katada, N. Ohashi, Y. Moriyoshi, and T. Ishigaki: Pyrogenic lron(III)-doped TiO_2 nanopowders synthesized in RF thermal plasma: Phase formation, defect structure, band gap, and magnetic properties. *J. Am. Chem. Soc.* **127**, 10982 (2005).
32. R.A. Spurr and H. Myers: Quantitative analysis of anatase-rutile mixtures with an x-ray diffractometer. *Anal. Chem.* **29**, 760 (1957).
33. J.G. Li, M. Ikeda, C.C. Tang, Y. Moriyoshi, H. Hamanaka, and T. Ishigaki: Chlorinated nanocrystalline TiO_2 powders via one-step Ar/O_2 radio frequency thermal plasma oxidizing mists of $TiCl_3$ solution: Phase structure and photocatalytic performance. *J. Phys. Chem. C* **111**, 18018 (2007).
34. J.C. Yu, J.G. Yu, W.K. Ho, Z.T. Jiang, and L.Z. Zhang: Effects of F-doping on the photocatalytic activity and microstructures of nanocrystalline TiO_2 powders. *Chem. Mater.* **14**, 3808 (2002).
35. A. Hagfeldt and M. Gratzel: Light-induced redox reaction in nanocrystalline system. *Chem. Rev.* **95**, 49 (1995).
36. E.E. Latta and M. Ronay: Catalytic oxidation of niobium. *Phys. Rev. Lett.* **53**, 948 (1984).
37. D. Morris, Y. Dou, J. Rebane, C.E.J. Mitchell, R.G. Egdell, D.S.L. Law, A. Vittadini, and M. Casarin: Photoemission and STM study of the electronic structure of Nb-doped TiO_2. *Phys. Rev. B* **61**, 13445 (2000).
38. C.L. Qiu, L. Liu, M. Sun, and S.M. Zhang: The effect of Nb addition on mechanical properties, corrosion behavior, and metal-ion release of ZrAlCuNi bulk metallic glasses in artificial body fluid. *J. Biomed. Mater. Res. Part A* **75**, 950 (2005).
39. J.D. Zhang, S. Fung, L.B. Lin, and Z.J. Liao: Ti ion valence variation induced by ionizing radiation at TiO_2/Si interface. *Surf. Coat. Tech.* **158**, 238 (2002).
40. C.R. Cho, J.P. Kim, J.Y. Hwang, S.Y. Jeong, Y.G. Joh, and D.H. Kim: High resolution elemental and magnetic distribution mapping and chemical bonding states of Co:TiO_2 films: A SAM, MFM and XPS study. *Jpn. J. Appl. Phys.* **43**, L1323 (2004).
41. F.A. Kröger and H.J. Vink: Relations between the concentrations of imperfections in crystalline solids. *Solid State Phys.* **3**, 307 (1956).
42. Y.L. Li and T. Ishigaki: Thermodynamic analysis of nucleation of anatase and rutile from TiO_2 melt. *J. Cryst. Growth* **242**, 511 (2002).
43. R.D. Shannon: Revised effective ionic-radii and systematic studies of interatomic distances in halides and chalcogenides. *Acta Crystallogr. A* **32**, 751 (1976).
44. H. Kamisaka, T. Hitosugi, T. Suenaga, T. Hasegawa, and K. Yamashita: Density-functional theory based first-principle calculation of Nb-doped anatase TiO_2 and its interactions with oxygen vacancies and interstitial oxygen. *J. Chem. Phys.* **131**, 034702 (2009).
45. H. Nogawa, T. Hitosugi, A. Chikamatsu, S. Nakao, Y. Hirose, T. Shimada, H. Kumigashira, M. Oshima, and T. Hasegawa: Carrier compensation by excess oxygen atoms in anatase $Ti_{0.94}Nb_{0.06}O_{2+\delta}$ epitaxial thin films. *Jpn. J. Appl. Phys.* **49**, 041102 (2010).
46. M.K. Akhtar, S.E. Pratsinis, and S.V.R. Mastrangelo: Dopants in vapor-phase synthesis of titania powders. *J. Am. Ceram. Soc.* **75**, 3408 (1992).
47. S. Ogata, H. Iyetomi, K. Tsuruta, F. Shimojo, A. Nakano, R.K. Kalia, and P. Vashishta: Role of atomic charge transfer on sintering of TiO_2 nanoparticles: Variable-charge molecular dynamics. *J. Appl. Phys.* **88**, 6011 (2000).
48. S. Hishita, I. Mutoh, K. Koumoto, and H. Yanagida: Inhibition mechanism of the anatase-rutile phase transformation by rare earth oxides. *Ceram. Int.* **9**, 61 (1983).
49. J.G. Li, X.H. Wang, H. Kamiyama, T. Ishigaki, and T. Sekiguchi: RF plasma processing of Er-doped TiO_2 luminescent nanoparticles. *Thin Solid Films* **506**, 292 (2006).
50. S. Vemury and S.E. Pratsinis: Dopants in flame synthesis of titania. *J. Am. Ceram. Soc.* **78**, 2984 (1995).
51. M.A. Barakat, G. Hayes, and S.I. Shah: Effect of cobalt doping on the phase transformation of TiO_2 nanoparticles. *J. Nanosci. Nanotechnol.* **5**, 759 (2005).
52. Y.H. Zhang, C.K. Chan, J.F. Porter, and W. Guo: Micro-Raman spectroscopic characterization of nanosized TiO_2 powders prepared by vapor hydrolysis. *J. Mater. Res.* **13**, 2602 (1998).
53. J.C. Parker and R.W. Siegel: Raman microprobe study of nanophase TiO_2 and oxidation-induced spectral changes. *J. Mater. Res.* **5**, 1246 (1990).
54. N. Serpone, D. Lawless, and R. Khairutdinov: Size effects on the photophysical properties of colloidal anatase TiO_2 particles-size quantization or direct transitions in this indirect semiconductor. *J. Phys. Chem.* **99**, 16646 (1995).
55. C. Kormann, D.W. Bahnemann, and M.R. Hoffmann: Preparation and characterization of quantum-size titanium-dioxide. *J. Phys. Chem.* **92**, 5196 (1988).
56. M.M. Rahman, K.M. Krishna, T. Soga, T. Jimbo, and M. Umeno: Optical properties and x-ray photoelectron spectroscopic study of pure and Pb-doped TiO_2 thin films. *J. Phys. Chem. Solids* **60**, 201 (1999).
57. J.G. Yu, J.C. Yu, W.K. Ho, and Z.T. Jiang: Effects of calcination temperature on the photocatalytic activity and photo-induced superhydrophilicity of mesoporous TiO_2 thin films. *N. J. Chem.* **26**, 607 (2002).
58. N. Daude, C. Gout, and C. Jouanin: Electronic band-structure of titanium-dioxide. *Phys. Rev. B* **15**, 3229 (1977).
59. J.G. Li, X. Yang, and T. Ishigaki: Urea coordinated titanium trichloride $Ti^{III}[OC(NH)_2]_6Cl_3$: A single molecular precursor yielding highly visible light responsive TiO_2 nanocrystallites. *J. Phys. Chem. B* **110**, 14611 (2006).
60. R.K. Sharma and M.C. Bhatnagar: Improvement of the oxygen gas sensitivity in doped TiO_2 thick films. *Sens. Actuators, B* **56**, 215 (1999).
61. M.R. Hoffmann, S.T. Martin, W.Y. Choi, and D.W. Bahnemann: Environmental applications of semiconductor photocatalysis. *Chem. Rev.* **95**, 69 (1995).
62. R.I. Bickley, T. Gonzalezcarreno, J.S. Lees, L. Palmisano, and R.J.D. Tilley: A structural investigation of titanium-dioxide photocatalysis. *J. Solid State Chem.* **92**, 178 (1991).

https://doi.org/10.1557/jmr.2011.16 Published online by Cambridge University Press